

This is the accepted manuscript made available via CHORUS. The article has been published as:

# Magnetic phase transitions and bulk spin-valve effect tuned by in-plane field orientation in $\text{Ca}_{\{3\}}\text{Ru}_{\{2\}}\text{O}_{\{7\}}$

D. Fobes, J. Peng, Z. Qu, T. J. Liu, and Z. Q. Mao

Phys. Rev. B **84**, 014406 — Published 20 July 2011

DOI: [10.1103/PhysRevB.84.014406](https://doi.org/10.1103/PhysRevB.84.014406)

# Magnetic phase transitions and bulk spin valve effect tuned by in-plane field orientation in $\text{Ca}_3\text{Ru}_2\text{O}_7$

D. Fobes, J. Peng, Z. Qu, T. J. Liu, and Z. Q. Mao\*

*Department of Physics, Tulane University, New Orleans, LA 70118*

(Dated: May 20, 2011)

We have performed systematic in-plane angle dependent  $c$ -axis transverse magnetotransport measurements on the double layered ruthenate  $\text{Ca}_3\text{Ru}_2\text{O}_7$  throughout a broad field and temperature range. Our results reveal the magnetic states unusually evolve with in-plane rotation of magnetic field. When magnetic field is applied along the  $b$ -axis we probe crossover magnetic states in close proximity to phase boundaries of long-range ordered antiferromagnetic (AFM) states. These crossover magnetic states are characterized by short-range antiferromagnetic order and switch to polarized paramagnetic states at critical angles as the in-plane field is rotated from the  $b$ - to  $a$ -axis. Additionally, we observe bulk spin valve behavior resulting from spin-flop transitions tuned by in-plane rotation of magnetic field. Our results highlight the complex nature of the spin-charge coupling in  $\text{Ca}_3\text{Ru}_2\text{O}_7$  and posts a challenging question: why does the change of magnetic field orientation result in magnetic phase transitions.

PACS numbers: 75.30.Kz, 71.27.+a, 75.47.-m, 75.30.Gw, 75.47.De

## I. INTRODUCTION

Layered ruthenates in the Ruddlesden-Popper series  $(\text{Sr,Ca})_{n+1}\text{Ru}_n\text{O}_{3n+1}$  exhibit exceptionally rich ground state properties, including unique physical phenomena such as unconventional spin-triplet superconductivity,<sup>1-3</sup> antiferromagnetic (AFM) Mott insulator behavior and orbital ordering,<sup>4-6</sup> itinerant metamagnetism with a field tuned nematic phase,<sup>7-9</sup> and orbital selective itinerant metamagnetism.<sup>10,11</sup> These unusually rich ground states headline the complex interplay between the charge, spin, lattice and orbital degrees of freedom in ruthenates, and provide fantastic opportunities to study the novel quantum phenomena tuned by non-thermal parameters like chemical doping, pressure, and magnetic field.

The double-layered calcium ruthenate  $\text{Ca}_3\text{Ru}_2\text{O}_7$  studied in this article has particularly interesting properties. It orders antiferromagnetically at  $T_N = 56$  K,<sup>12,13</sup> where moments are ferromagnetically ordered in the bilayers coupled antiferromagnetically along the  $c$ -axis.<sup>14</sup> The AFM phase transition is closely followed by a first order metal-insulator (MI) transition at  $T_{\text{MIT}} = 48$  K,<sup>12,13</sup> with a quasi-two-dimensional metallic state observed for  $T < 30$  K.<sup>15,16</sup> Photoconductivity and Raman spectroscopy measurements revealed the MI transition to be associated with the opening of a charge gap<sup>15,17</sup> and suggested orbital ordering.<sup>17-19</sup> Resonant x-ray scattering studies suggest that while the orbital order parameter in  $\text{Ca}_3\text{Ru}_2\text{O}_7$  is substantially weaker than in  $\text{Ca}_2\text{RuO}_4$ , weak orbital order combined with strong spin-orbit coupling lead to the rich ground state properties of  $\text{Ca}_3\text{Ru}_2\text{O}_7$ .<sup>20</sup> Angle resolved photoemission spectroscopy measurements further revealed that while large portions of the Fermi surface are indeed gapped below  $T_{\text{MIT}}$ , some small metallic, non-nested pockets survive.<sup>16</sup> With the application of magnetic field,  $\text{Ca}_3\text{Ru}_2\text{O}_7$  undergoes a remarkable anisotropic transition in magnetoresistivity. At 2 K when magnetic field is applied along the in-plane

easy-axis ( $b$ -axis), giant magnetoresistance is observed at  $B_c \sim 6$  T.<sup>21</sup> However, for fields along the in-plane hard-axis ( $a$ -axis), colossal magnetoresistance is observed for much greater magnetic fields ( $B_c > 15$  T).<sup>19,21</sup> The giant/colossal magnetoresistance has previously been attributed to the bulk spin-valve effect resulting from a spin-flop transition.<sup>22,23</sup> However, the bulk spin-valve effect model alone cannot explain why the larger colossal magnetoresistance is observed for fields along the hard-axis, contrary to general expectations for a spin-valve model.

Recent single crystal neutron scattering studies have resolved this puzzle by revealing the different magnetic structures under magnetic fields applied along the  $b$ -axis.<sup>24</sup> Below the spin-flop transition field  $B_c$ , the probed AFM structure is consistent with the model previously proposed for  $\text{Ca}_3\text{Ru}_2\text{O}_7$  by DFT calculations<sup>23</sup> and powder neutron diffraction studies,<sup>14</sup> *i.e.* FM bilayers, with magnetic moments oriented along the  $b$ -axis, are stacked antiferromagnetically along the  $c$ -axis (This phase was labeled AFM-b in Ref. 24). However, above the spin-flop transition the antiferromagnetically-coupled FM bilayers do not switch to a fully polarized FM state as expected in a typical spin-valve model. Instead, the system enters a canted AFM state (labeled CAFM), above  $B_c$ , where the spins of alternating bilayers are canted  $25^\circ$  from the  $b$ -axis. In addition, the AFM structure between  $T_N$  and  $T_{\text{MIT}}$  is found to be distinct from AFM-b, having an in-plane easy-axis along the  $a$ -axis instead (thus being labeled AFM-a). We will use the same notations, *i.e.* AFM-a, AFM-b and CAFM to describe these various magnetic states in our following discussions.

In this article, we have systematically investigated the anisotropic properties of various magnetic states of  $\text{Ca}_3\text{Ru}_2\text{O}_7$  through measurements of in-plane angular dependence of  $c$ -axis transverse magnetoresistivity  $\rho_c(B, \phi)$  throughout a wide temperature and field range. Our data reveals that the nature of magnetic state of  $\text{Ca}_3\text{Ru}_2\text{O}_7$  is

dependent on the orientation of magnetic field. The magnetic phase diagram is much more complex for  $H//b$  than  $H//a$ . Crossover magnetic states characterized by short-range AFM or CAFM order are probed in close proximity to the AFM-a, AFM-b and CAFM phase boundaries for  $H//b$ . We observe several different types of magnetic phase transition as the in-plane magnetic field is rotated from the  $b$ - to  $a$ -axis, including the AFM-b-to-CAFM spin-flop transition which results in a bulk spin valve effect. These results indicate that the spin and charge degrees of freedom are strongly coupled in this system and that spin degree of freedom of correlated electrons can be manipulated by magnetic field orientation.

## II. EXPERIMENT

The crystals used in this study were grown by floating zone technique and shown to be pure  $\text{Ca}_3\text{Ru}_2\text{O}_7$  by x-ray diffraction and are free of twin-domains. Magnetization measurements performed with magnetic field oriented along the  $a$ -axis and  $b$ -axis were used to exclude the presence of twin-domains in the samples, which would result in the spin-flop transitions at 6 T to appear for fields aligned along both of the primary in-plane crystallographic axes. Crystal orientation was determined using Laue X-ray diffraction. The sample used in this study is approximately disk-shaped with a diameter of  $\sim 0.77$  mm and thickness of  $\sim 0.15$  mm. The  $c$ -axis resistivity at 2 K under no magnetic field is  $0.66 \Omega\text{-cm}$ . Our magnetoresistivity anisotropy and DC magnetization measurements were performed with a Physical Property Measurement System (PPMS, Quantum Design). The resistivity measurements were conducted with a standard four probe technique, where the electrodes for the current leads are shaped as an unclosed circle in order to distribute current more uniformly and the electrodes for the voltage leads were placed at the center of the circle on both the top and bottom surfaces of the sample.

## III. RESULTS AND DISCUSSION

In figure 1(a) and 1(b) we present the magnetic phase diagram for magnetic fields applied to the  $a$ - and  $b$ -axes, respectively, constructed from systematic measurements of magnetoresistivity as a function of temperature, magnetic field and in-plane orientation of magnetic field. The phase diagram for  $B//a$  is relatively simple and is consistent with that established in previous work using flux grown single crystals.<sup>25</sup> We observe a single magnetic transition at critical field  $B_c$  in field sweep measurements at fixed temperatures, as shown in Fig. 2. This transition corresponds to a second-order spin-flop transition from an AFM-a state to an enhanced paramagnetic state (EPM) for  $48 \text{ K} < T < 56 \text{ K}$ , and to a nearly first-order spin-flop transition from a AFM-b state to an EPM state for  $T < 48 \text{ K}$ . The critical temperature  $T_{\text{MIT}}$  shown in

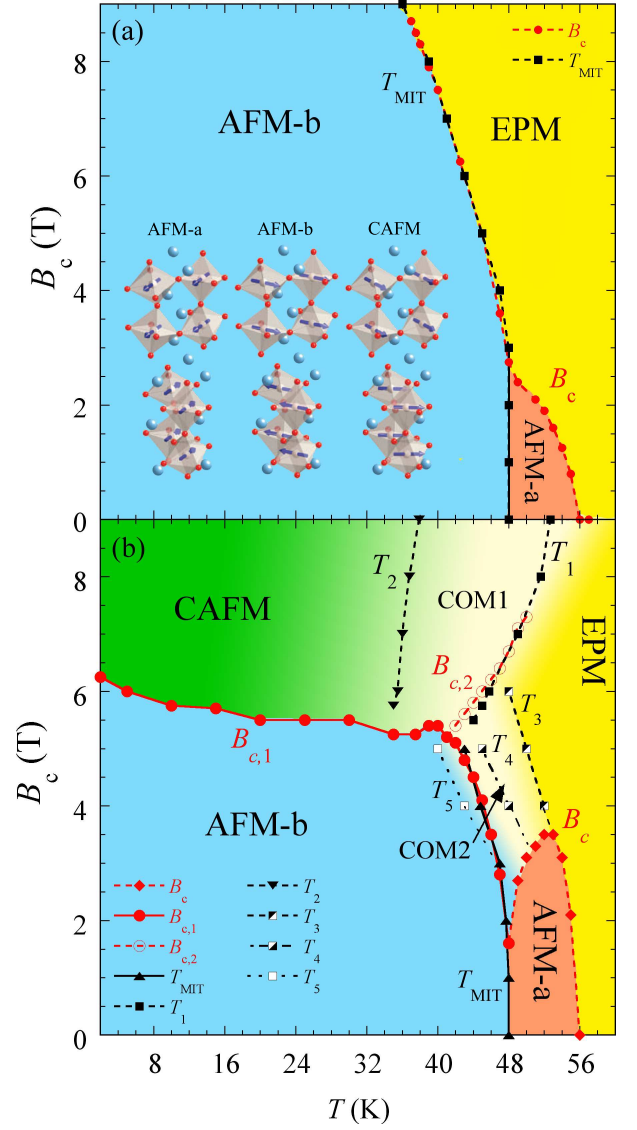


FIG. 1: (Color Online) Magnetic phase diagram developed from interplanar ( $\rho_c$ ) transport as a function of temperature and magnetic field. Phase boundaries are formed by critical magnetic fields and temperatures of spin flip/flop transitions, along the  $a$ - (a) and  $b$ -axis (b). We utilize similar notation used in Ref. 24, i.e. AFM-a, AFM-b and CAFM to label various magnetic states. AFM-a represents the AFM state with magnetic moments along the  $a$ -axis; AFM-b represents the AFM state with magnetic moments along the  $b$ -axis; CAFM represents a canted AFM state where spins in the bilayers are canted  $25^\circ$  from the  $b$ -axis. The inset in (a) shows schematic magnetic structures of these phases<sup>24</sup>. EPM in both (a) and (b) denotes enhanced paramagnetic states. In close proximity to the AFM-a and AFM-b phase boundaries for  $B//b$ , we observe a crossover magnetic state, denoted by COM2;  $T_3$ ,  $T_4$  and  $T_5$  represents the critical temperatures where the magnetoresistivity anisotropy of  $\rho_c(B, \phi)$  shows critical changes (see Fig. 10 and the text).  $T_{\text{MIT}}$  in both (a) and (b) represents the metal-insulator transition temperature. COM1 in (b) represents the crossover magnetic state between the CAFM and EPM states.  $T_1$  and  $T_2$  are characteristic temperatures where the curvature of the temperature dependence of magnetoresistivity  $\rho_c(T)$ , as well as the magnetoresistivity anisotropy, shows remarkable changes (see Fig. 5 and 10)

Fig. 1(a) represents the metal-insulator transition temperatures identified in temperature sweep measurements at fixed magnetic fields (see Fig. 3). The phase boundaries defined by  $T_{\text{MIT}}$  and  $B_c$  overlap when  $T < 48$  K.

The phase diagram for  $B\parallel b$  (Fig. 1(b)) is much more complex. As revealed in previous neutron scattering studies, the spin-flop transition at low temperature for  $B\parallel b$  is distinct from that for  $B\parallel a$ ; a CAFM state occurs above the spin-flop transition field.<sup>24</sup> The magnetic structure of the CAFM state is presented in the inset of Fig. 1(a), where the magnetic structures of AFM-a and AFM-b states are also given for comparison. The critical fields  $B_{c,1}$  for this spin flop transition probed in our magneto-transport measurements (see Fig. 4) are consistent with those determined by neutron scattering measurements. When  $40 \text{ K} \leq T \leq 50 \text{ K}$ , double magnetic transitions are observed in the field sweep measurements; they are denoted by  $B_{c,1}$  (medium arrows) and  $B_{c,2}$  (long arrows) respectively in Fig. 4 and Fig. 1(b). For  $B < 6$  T, the  $B_{c,1}$  boundary is accompanied by metal-insulator transition, similar to the scenario of  $T < 48$  K for  $B\parallel a$ .  $T_{\text{MIT}}$  in Fig. 1(b) represents the metal-insulator transition temperature measured in temperature sweep measurements of magnetoresistivity at fixed magnetic fields (see Fig. 5). For  $B > 6$  T, we observe a crossover magnetic state between CAFM and EPM (i.e. the COM1 state in Fig. 1(b)). The critical temperatures  $T_1$  and  $T_2$  represent the boundaries of this crossover magnetic phase defined from striking changes in the slopes of magnetoresistivity as a function of temperature ( $\rho_c(T)$ ), as shown in the inset of Fig. 5. Magnetoresistivity as a function of field also shows noticeable slope changes near the  $T_1$  phase boundary, as shown by the critical field  $B_{c,2}$  in the diagram; the  $B_{c,2}$  boundary agrees well with the  $T_1$  boundary. Moreover, the magnetoresistivity anisotropy of  $\rho_c(B, \phi)$  also displays critical changes near  $T_1$  and  $T_2$  as shown below. Our discussions given below suggests that this crossover magnetic state is characterized by short-range CAFM order. In addition, in close proximity to the boundaries of the AFM-a and AFM-b phases, we find another crossover magnetic state between  $T_3$  and  $T_5$  (indicated by COM2 in Fig. 1(b)), which is characterized by short-range AFM order as we discuss below.  $T_3$  and  $T_5$ , as well as  $T_4$ , are defined as characteristic temperatures where the magnetoresistivity anisotropy show critical changes (see Fig. 10). Among the magnetic phase transitions shown in Fig. 1(b), only the transition at  $B_{c,1}$  corresponds to a first-order spin flip/flop transition, while the transitions at  $B_{c,2}$  (or  $T_1$ ),  $T_2$ ,  $T_3$ ,  $T_4$  and  $T_5$  all correspond to either second-order or crossover transitions. This can clearly be seen in the contour plot of resistivity as a function of temperature and magnetic field shown in Fig. 6, where critical fields and critical temperatures in Fig. 1(b) have also been included.

Since the magnetic phase diagrams for  $B\parallel a$  and  $B\parallel b$  are distinct, as seen in Fig. 1, magnetic phase transitions tuned by in-plane orientation angle of magnetic field can be expected. To reveal the nature of such mag-

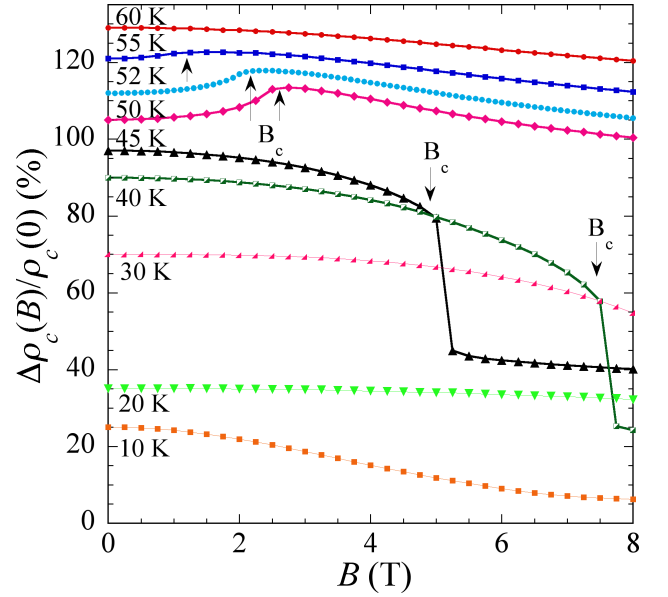


FIG. 2: (Color Online) Magnetic field dependence of normalized transverse  $c$ -axis magnetoresistivity  $\Delta\rho_c(B)/\rho_c(0)$  at various temperatures, measured with magnetic field applied along the  $a$ -axis. Arrows indicate critical fields for spin-flop transitions  $B_c$ , determined by identifying the field at which  $|d\rho_c(B)/dB|$  is a maximum. Data has been normalized and shifted for clarity.

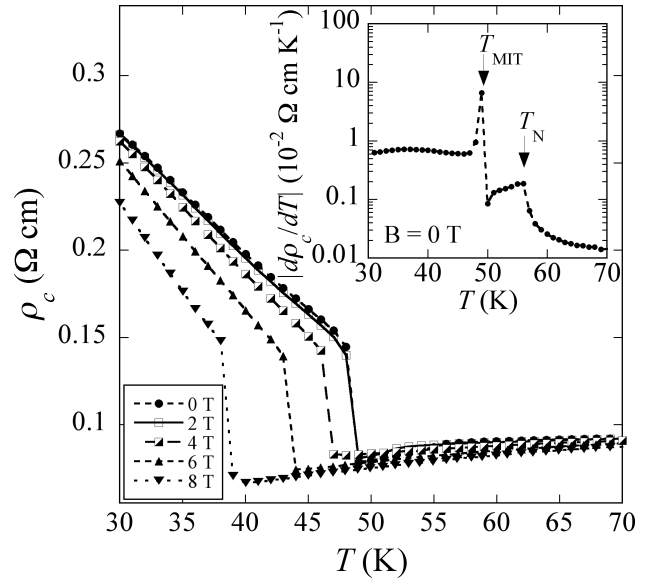


FIG. 3: Temperature dependence of transverse  $c$ -axis magnetoresistivity ( $\rho_c(T)$ ) at typical fields, measured with magnetic field applied along the  $a$ -axis. Inset: temperature dependence of derivative of resistivity with respect to temperature ( $|d\rho_c/dT|(T)$ ) at zero field.  $T_{\text{MIT}}$  under various magnetic fields is determined by identifying the temperature at which  $|d\rho_c/dT|(T)$  is a maximum.



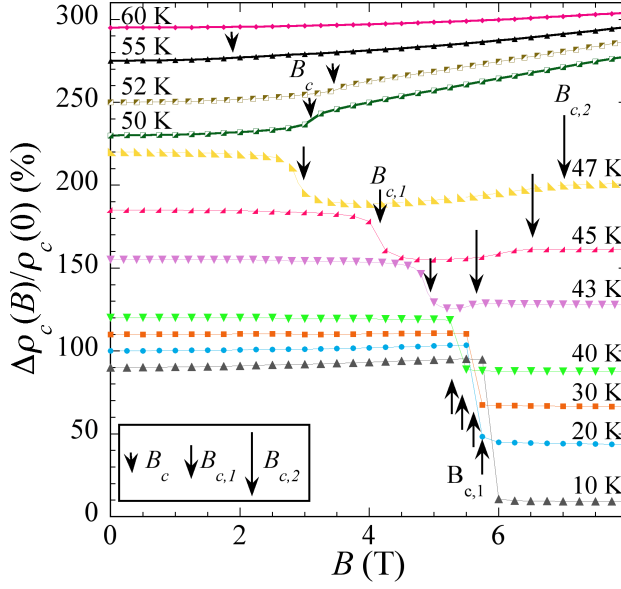


FIG. 4: (Color Online) Magnetic field dependence of transverse  $c$ -axis magnetoresistivity ( $\rho_c(B)$ ) at typical temperatures, measured with magnetic field applied along the  $b$ -axis. Arrows indicate critical fields for different spin flip/flop transitions,  $B_c$ ,  $B_{c,1}$ , and  $B_{c,2}$  (see text for details). Data has been normalized and shifted for clarity.

netic transitions, we have performed systematic measurements on the in-plane angular dependence of the  $c$ -axis magnetoresistivity  $\rho_c(B, \phi)$  at various temperatures and fields, crossing various phase boundaries established for  $B \parallel a$  and  $B \parallel b$  in Fig. 1. The inset to Fig. 7 shows a schematic of in-plane field rotation.  $\rho_c(B, \phi)$  displays a variety of characteristics, depending on temperature and magnetic field as presented below; this implies that the rotation of in-plane magnetic field leads the magnetic state to undergo various evolutions. To summarize, we observe four different types of evolution, three types of which correspond to remarkable magnetic phase transitions. To clearly address these evolutions, we denote the magnetic state with  $H \parallel b$  as an initial state and the magnetic state with  $H \parallel a$  as a final state, and only consider  $90^\circ$  rotation from the  $b$ - to  $a$ -axis in related discussions. The nature of the evolution of the magnetic state depends on the initial state in the  $H \parallel b$  phase diagram (Fig. 1b) as described below:

When the initial state resides in the AFM-b phase (see Fig. 1b) and is not close to the  $B_{c,1}$  phase boundary, in-plane rotation of field does not lead to any spin flip/flop transition; the system remains AFM-b during the entire rotation from the  $b$ - to  $a$ -axis. In this case,  $\rho_c(B, \phi)$  exhibits twofold anisotropy as shown in the data collected at 1 T and  $T < 45$  K in Fig. 7, and can be fitted to a sine-squared function. Such anisotropy can be attributed to Ising-type anisotropy, which is often observed in other magnetic systems with Ising-type anisotropy.<sup>26–29</sup> Ising-type anisotropy is also observed in  $\rho_c(B, \phi)$  when the

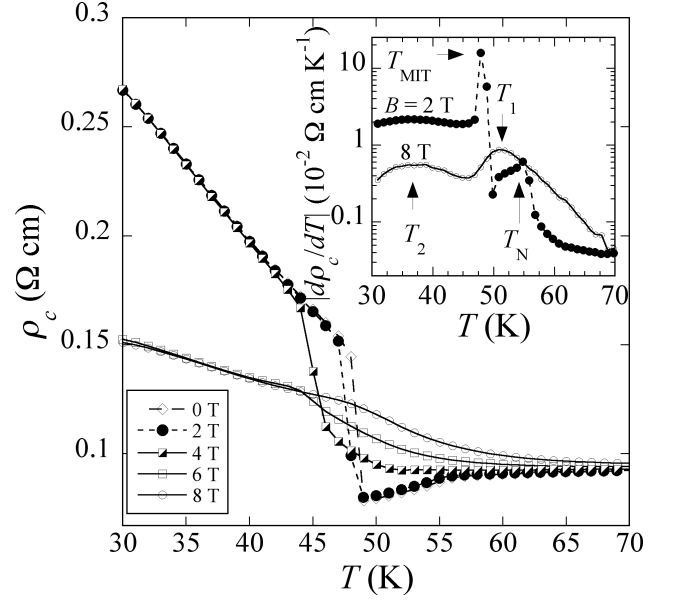


FIG. 5: Temperature dependence of transverse  $c$ -axis magnetoresistivity ( $\rho_c(T)$ ) at typical fields, measured with magnetic field applied along the  $b$ -axis. Inset: temperature dependence of derivative of resistivity with respect to temperature ( $|d\rho_c/dT|(T)$ ) at 2 T and 8 T.

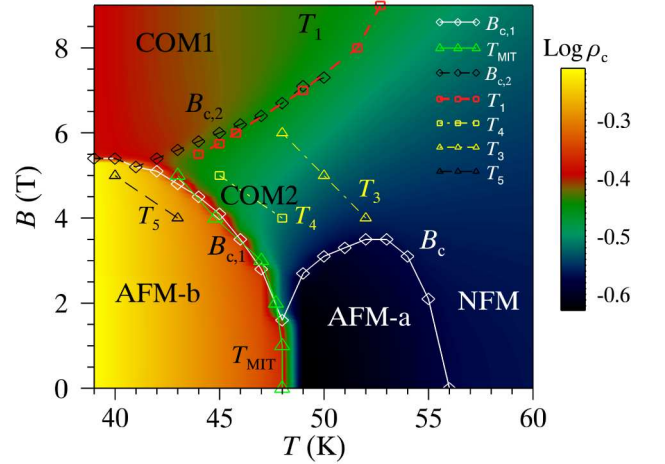


FIG. 6: (Color Online) Contour plot of  $c$ -axis resistivity  $\rho_c$  on the log scale as a function of magnetic field ( $\parallel b$ -axis, upward sweep) and temperature near the metal-insulator transition. AFM-a and AFM-b represent the antiferromagnetic phase with the easy-axis along the  $a$ - and  $b$ -axes respectively; COM1 and COM2 denote the crossover magnetic states; EPM stands for the enhanced paramagnetic phase.

initial state is AFM-a (see Fig. 1b) or enhanced paramagnetic state (EPM in Fig. 1b), as seen from the data collected at 1 T and  $T > 45$  K. Interestingly, we observe a phase shift of  $\pi/2$  in  $\rho_c(B, \phi)$  anisotropy when the initial state is across the EPM/AFM-a or the AFM-a/AFM-b phase boundary. The minima of magnetoresistivity is along the  $a$ -axis in the EPM phase (see the top panel

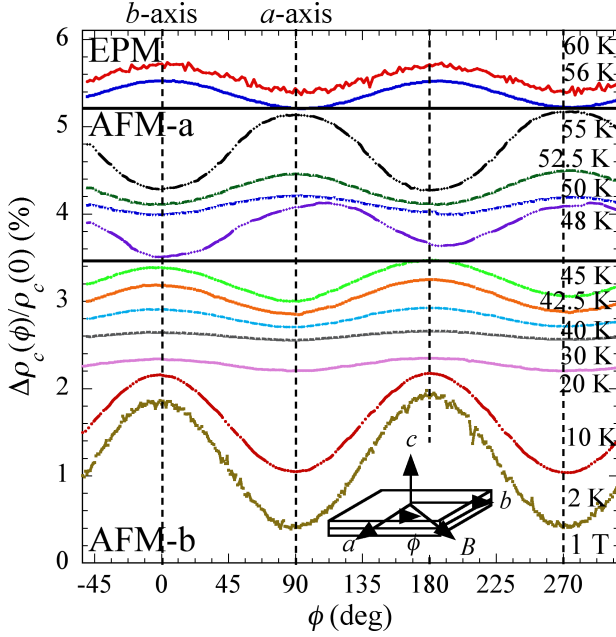


FIG. 7: (Color Online) In-plane angular dependence of magnetoresistivity at selected temperatures at an applied magnetic field of 1 T. The system is EPM above  $T_N$  (top panel), AFM-a for  $T_{MIT} < T < T_N$  (center panel), and AFM-b for  $T \leq T_{MIT}$  (bottom panel). Data has been normalized and shifted for clarity. The inset illustrates the in-plane rotation of magnetic field.

in Fig. 7), but shifts to the  $b$ -axis for the AFM-a phase (see the middle panel in Fig. 7) and back to the  $a$ -axis for the AFM-b phase (see the bottom panel in Fig. 7). Besides the phase shifts, the amplitude of the anisotropy also exhibits a non-monotonic temperature dependence; remarkable maximal amplitudes are observed near both boundaries.

Such an evolution of magnetoresistivity anisotropy through EPM, AFM-a and AFM-b phases can be well understood in light of magnetic structures of these phases revealed in previous studies.<sup>14,23–25</sup> As indicated above, both AFM-a and AFM-b phases have A-type antiferromagnetic structure (see the inset to Fig. 1(a)), i.e. FM bilayers are antiferromagnetically coupled along the  $c$ -axis. Magnetic moments are along the  $a$ -axis (i.e. in-plane easy-axis) for AFM-a and along the  $b$ -axis (in-plane easy-axis) for AFM-b. Such a switch of magnetic easy-axis across the AFM-a/AFM-b phase boundary was initially identified in magnetization measurements by Cao *et al.*,<sup>12</sup> and later confirmed by neutron scattering measurements.<sup>14,24</sup> Neutron scattering studies have also revealed that the giant/colossal magnetoresistance originates from the spin flop transition from the AFM-b to CAFM phase<sup>24</sup>. This indicates that interlayer spin scattering dominates electronic transport properties in  $\text{Ca}_3\text{Ru}_2\text{O}_7$ . Thus the maximal value of the  $c$ -axis magnetoresistivity should occur when the magnetic field is rotated to the magnetic easy-axis where antiparallel spin

alignment between bilayers is most preferred, which maximize spin scattering between layers. Since the in-plane magnetic easy-axis is along the  $a$ -axis for the AFM-a phase and the  $b$ -axis for the AFM-b phase, we can naturally expect that the magnetoresistivity reaches a maximum as the field is rotated to the  $a$ -axis for the AFM-a phase and the  $b$ -axis for the AFM-b phase. Thus it is not surprising to observe the  $\pi/2$  phase shift in  $\rho_c(B, \phi)$  when the magnetic state switches from the AFM-a to AFM-b. From our recent inelastic neutron scattering measurements, we find that the interlayer antiferromagnetic coupling strength is extremely weak compared to the intralayer ferromagnetic coupling strength.<sup>30</sup> Given such weak interlayer AFM coupling, we can reasonably assume that the system is dominated by quasi-two-dimensional FM fluctuations before it enters an AFM-a state, which is actually manifested in the positive Curie-Weiss temperature of  $\text{Ca}_3\text{Ru}_2\text{O}_7$ .<sup>31</sup> The sine-squared anisotropy in magnetoresistivity of this magnetic state is consistent with experimentally observed and theoretically predicted FM anisotropy for similar crystallographic symmetry. We also note that the  $c$ -axis magnetoresistivity  $\Delta\rho_c(B)/\rho_c(0)$  of the EPM phase is negative for  $B\parallel a$  (e.g. see the data at 60 K in Fig. 2), but positive for  $B\parallel b$  (e.g. see the data at 60 K in Fig. 4), which implies that the in-plane Ising easy-axis is the  $a$ -axis for the EPM phase; this is consistent with the fact that magnetic moments are aligned along the  $a$ -axis when the system evolves into the AFM-a phase.

The non-monotonic temperature dependence of the amplitude of magnetoresistivity anisotropy stated above (see Fig. 7) can be further interpreted in terms of competing effects of intralayer and interlayer magnetic coupling on  $c$ -axis transport in various magnetic phases. In the following discussions, we use  $J_{\parallel}$  and  $J_{\perp}$  to denote intralayer and interlayer magnetic coupling strength respectively. Anisotropy arising from  $J_{\parallel}$  and  $J_{\perp}$  is out of phase by  $\pi/2$ , therefore as  $J_{\parallel}$  and  $J_{\perp}$  competitively affect  $\rho_c$  transport, their respective anisotropies interfere destructively. This can be understood as following. In the EPM state, since the system is dominated by quasi-two-dimensional ferromagnetic fluctuations and  $J_{\perp}$  is nearly negligible, the  $c$ -axis magnetoresistivity is thus expected to be minimal as the field is rotated to the magnetic easy-axis (i.e.  $a$ -axis), where spin polarization is maximal. Our observation of the anisotropy of magnetoresistivity for the EPM state exactly fits into this expected scenario; we indeed observe minimum magnetoresistivity when the field is oriented along the  $a$ -axis. In other words,  $J_{\parallel}$  results in twofold magnetoresistivity anisotropy with the minimum occurring along the  $a$ -axis. For the AFM-a or AFM-b phases,  $J_{\perp}$  cannot be ignored despite it being very weak; it plays a pivotal role in establishing long-range ferromagnetic order within the plane. When the magnetic field is rotated to the easy-axis (the  $a$ -axis for the AFM-a phase, the  $b$ -axis for the AFM-b phase), the antiparallel spin alignment between layers is most preferred. In this case, the

spin scattering rate is maximal as pointed out above, thus leading to the maximal magnetoresistivity. The magnetoresistivity anisotropy is clearly dominated by  $J_{\perp}$  under this circumstance; we could say that  $J_{\perp}$  causes twofold magnetoresistivity anisotropy with the maximum occurring along the  $a(b)$ -axis for the AFM- $a(b)$ . The non-monotonic temperature dependence of the magnitude of magnetoresistivity anisotropy indeed reflects the competition between two anisotropies with the  $\pi/2$  phase shift, caused by  $J_{\parallel}$  and  $J_{\perp}$  respectively. In the EPM phase, the sine-squared anisotropy primarily arises from  $J_{\parallel}$ , as indicated above. The amplitude of this anisotropy is expected to increase with decreasing temperature, however, as the temperatures approaches  $T_N$ , the effects of  $J_{\perp}$  on the anisotropy cannot be ignored. Since the anisotropy resulting from  $J_{\perp}$  also has twofold symmetry, but is out of phase by  $\pi/2$  with respect to the anisotropy arising from  $J_{\parallel}$ , the superposition of such two anisotropy components leads to the non-monotonic temperature dependence of the amplitude. A similar mechanism also works for both the AFM- $a$  and AFM- $b$  phases. In contrast to the EPM phase, in the AFM- $a$  and AFM- $b$  phases,  $J_{\perp}$  plays the dominant role. In the AFM- $a$  phase, the maximal amplitude immediately below  $T_N$  is clearly the consequence of competition between anisotropy arising from  $J_{\perp}$  and  $J_{\parallel}$ . On the other hand, the maximal amplitude at the AFM- $a$ /AFM- $b$  boundary is ascribed to a significant increase of  $J_{\perp}$ , resulting from a remarkable increase of the ordered magnetic moment at this boundary, probed in neutron scattering measurements.<sup>24</sup> The decreases in amplitude in both the AFM- $a$  and AFM- $b$  phases are related to strengthening of  $J_{\parallel}$  with decreasing temperature. Below 30 K, the upturn in the amplitude indicates that  $J_{\perp}$  strengthens at lower temperatures, which is further supported by the large increase in interplanar spin scattering in this region, as evidenced by the significant increase in the difference between interplanar and intraplanar resistivity below the metal-insulator transition.<sup>32</sup>

If the initial magnetic state is CAFM (dark green region in Fig. 1b), in-plane rotation of field from  $b$ - to  $a$ -axis results in a CAFM-to-AFM- $b$  magnetic phase transition, which can easily be seen from the difference between the  $B\parallel a$  and  $B\parallel b$  phase diagrams in Fig. 1. Since the CAFM state is mostly polarized,<sup>24</sup> the spin flop transition from the CAFM to the unpolarized AFM- $b$  phase leads to a significant change in magnetoresistivity; this is manifested as discontinuous jumps in  $\rho_c(\phi)$  curves collected at 8 T and  $T < 40$  K, as shown in Figure 8 (see the bottom panel).

To further examine such an angle-tuned bulk spin-valve effect, we performed measurements of in-plane angular dependence of  $\rho_c$  at 2 K at various magnetic fields, shown in Figure 9. Below the spin-flop transition field  $B_{c,1} \sim 6.25$  T, we observe a sine-squared anisotropy with a minima along the  $a$ -axis (e.g. see the data at 1, 3, 5 and 6 T). This magnetoresistivity anisotropy arises from the in-plane Ising-type anisotropy of the AFM- $b$  magnetic state as described above. The magnetic state remains in

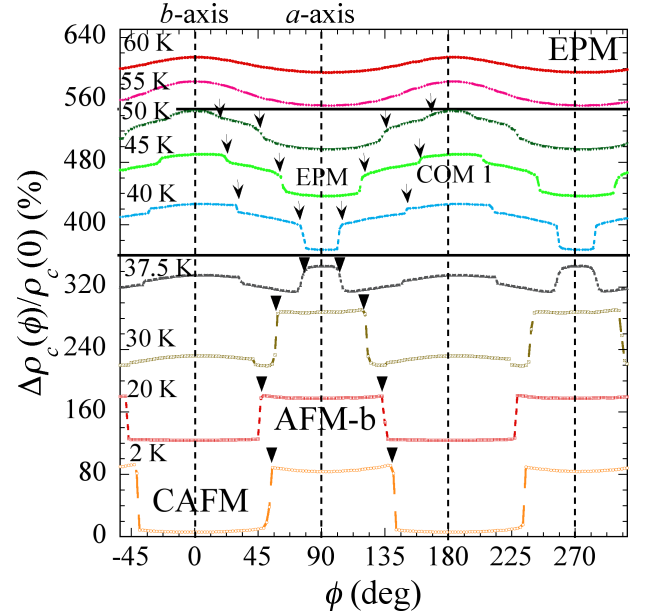


FIG. 8: (Color Online) In-plane angular dependence of  $c$ -axis magnetoresistivity at selected temperatures at an applied magnetic field of 8 T. The system is EPM in the whole angle range above 50 K (top panel). For  $40 \text{ K} \leq T \leq 50 \text{ K}$  the system is in the COM1 state when magnetic field is near the  $b$ -axis and in the EPM state when field is near the  $a$ -axis. When  $T < 40 \text{ K}$  the systems is in the CAFM state when field is near the  $b$ -axis and AFM- $b$  state when field is near the  $a$ -axis. Data has been normalized and shifted for clarity.

the AFM- $b$  phase as the in-plane field is rotated from the  $a$ - to  $b$ -axis for  $B < B_{c,1}$ , as shown in phase diagram of Fig. 1. Above  $B_{c,1}$  we observe the square-wave-like anisotropy (see the data at 7 and 8 T). At 7 T the sharp drop in magnetoresistivity occurs at  $|\phi_c| = 25^\circ$  from the  $b$ -axis as the angle sweeps from  $-a$  to the  $b$ -axis.  $|\phi_c|$  increases with increasing magnetic field, up to  $39^\circ$  at 8 T. We note that the component of applied magnetic along the  $b$ -axis is 6.34 T at  $\phi_c$  for the applied field of 7 T and 6.22 T at  $\phi_c$  for the applied field of 8 T. Both are close to the spin-flop transition field  $B_{c,1} (= 6.25 \text{ T})$  for  $B\parallel b$ . Additionally, from the data of 7 and 8 T, we note that the magnetoresistivity shows a sine-squared dependence once the system switches to the high resistive AFM- $b$  state. These results provide additional support for our argument that the giant magnetoresistance tuned by field and the field orientation has the same origin; both result from the spin-flop transition between the AFM- $b$  and CAFM magnetic states. Another noteworthy feature in Fig. 9 is that the square-wave-like anisotropy for  $B = 7 \text{ T}$  and 8 T is asymmetric about the  $b$ -axis; this can be attributed to the hysteresis of the first-order CAFM/AFM- $b$  phase transition.

If the initial magnetic state is in Crossover Region 1 (COM1 in Fig. 1b), which lies between CAFM and EPM, in-plane rotation of field leads to double magnetic phase transitions, manifested as double jumps in  $\rho_c(\phi)$  curves

(see the data at 40, 45 and 50 K in Figure 8). The COM1 state evolves to the EPM state via an intermediate magnetic state. Since the magnetoresistivity drops sharply as the magnetic state switches from the COM1 to the EPM, the COM1 phase is clearly less polarized than the EPM phase, suggesting that interlayer AFM coupling should exist throughout the COM1 region. The greater magnetoresistivity of this region can be attributed to interlayer spin scattering. However, previous neutron scattering measurements did not reveal any long-range CAFM order in the COM1 region<sup>24</sup>, indicating that the CAFM may exist as a short-range ordered state in this region.

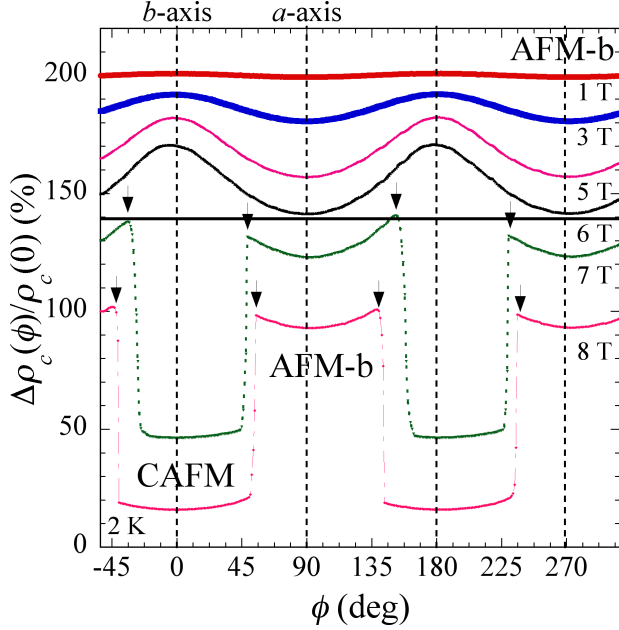


FIG. 9: (Color Online) In-plane angle dependence of  $\rho_c$  magnetoresistivity at selected magnetic fields at 2 K. The system is in the AFM-b phase for  $B \leq 6$  (top panel). When  $B > 6$  T the system is in the CAFM state when field is near the  $b$ -axis and AFM-b state when field is near the  $a$ -axis. Arrows indicate the critical angles  $\phi_c$  for spin-flop transitions. Data has been normalized and shifted for clarity.

When the initial magnetic state is Crossover Region 2 (COM2, the region between  $T_3$  and  $T_5$  in Fig. 1b), magnetic phase transitions tuned by the in-plane rotation of magnetic field are also observed. At temperatures between  $T_3$  and  $T_4$ , the magnetoresistivity shows a single drop at a critical angle as the magnetic field is rotated from the  $b$ - to  $a$ -axis as shown by the data taken at  $T = 46, 48$  and  $50$  K under the magnetic field of 5 T in Fig. 10 (indicated by downward arrows), indicating that the COM2 state with  $B \parallel b$  differs from the EPM state with  $B \parallel a$ . The greater magnetoresistivity of this state implies that it involves short-range AFM order. At temperatures between  $T_4$  and  $T_5$ , the magnetic state is in the AFM-b phase for  $B \parallel a$  (see Fig. 1a), but either in the COM2 or the AFM-b for  $B \parallel b$  (see Fig. 1b). The magnetic phase transition between  $B \parallel a$  and  $B \parallel b$  occurs

via an intermediate magnetic phase in this temperature range. As shown in Fig. 10, at  $T = 41$  K and  $42$  K, although the magnetic state is in the AFM-b for both  $B \parallel a$  and  $B \parallel b$  double magnetic transitions (indicated by upward arrows) happen as the magnetic field is rotated from the  $b$ - to  $a$ -axis, implying the presence of an intermediate magnetically ordered phase. The magnetoresistivity of this intermediate state is 25–35% smaller than that of the AFM-b phase with  $B \parallel a$  or  $B \parallel b$ , suggesting that it is strikingly polarized compared to the AFM-b. We note that previous studies by McCall *et al.*<sup>25</sup> reported a unique state in a similar temperature and field region where we observe the COM2 state. Their magnetization measurements reveal that this state is 50% polarized<sup>19,25</sup>, which is also confirmed in our magnetization measurements (data not shown here).

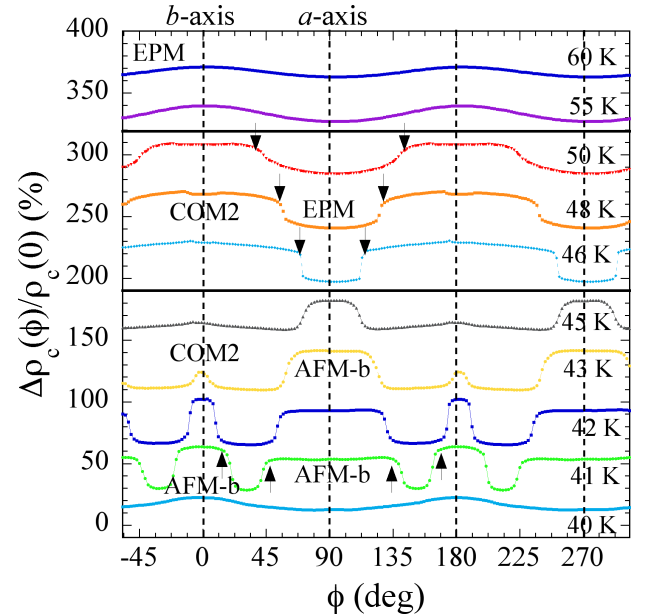


FIG. 10: (Color Online) In-plane angular dependence of transverse  $c$ -axis magnetoresistivity at selected temperatures at an applied magnetic field of 5 T. For  $T > 50$  K the system is EPM for the whole angle range (top panel). When  $46$  K  $\leq T \leq 50$  K, the system is in the COM2 state when field is near the  $b$ -axis and EPM state when field is near the  $a$ -axis (center panel). When  $41$  K  $\leq T \leq 45$  K, the system is in either the COM2 or AFM-b state when field is near the  $b$ -axis and AFM-b state when field is near the  $a$ -axis (bottom panel). For  $T \leq 40$  K the system is AFM-b in the whole angle range. Data has been normalized and shifted for clarity.

Magnetic phase transition tuned by magnetic field orientation is not a common phenomenon, as far as we know. Our observation of complex magnetic phase transitions tuned by the in-plane rotation of magnetic field stated above suggests that the spin degree of freedom, which is strong coupled with charge degree of freedom, is easily manipulated by the orientation of magnetic field. This can possibly be attributed to the unique anisotropic magnetic coupling in  $\text{Ca}_3\text{Ru}_2\text{O}_7$ . As we pointed out above,



the interlayer magnetic AFM coupling  $J_{\perp}$ , while it plays a critical role in establishing long-range AFM or CAFM order, is extremely weak compared to intralayer FM coupling. Given such small  $J_{\perp}$  we can naturally expect that small or moderate magnetic field can drive the AFM state to a polarized state. The spin flop transition from AFM-b to CAFM observed at  $\sim 6.25$  T for  $H\parallel b$  is exactly consistent with this expected scenario. The intermediate magnetic states we observed between magnetic phase transitions tuned by the in-plane rotation of magnetic field suggest that other intermediate polarized magnetic states also exist and that these polarized states are sensitive to field orientation. Further understanding of these phenomena requires systematic theoretical investigation.

#### IV. CONCLUSION

Using in-plane angle dependent  $c$ -axis magnetotransport measurements we have probed crossover magnetic states between the CAFM/AFM-b and the EPM phases for  $B\parallel b$  in  $\text{Ca}_3\text{Ru}_2\text{O}_7$ . These crossover magnetic states are characterized by short-range AFM/CAFM order and are polarized to the EPM state as the field is oriented close to the  $a$ -axis. We also observe bulk spin-valve effects arising from the AFM-b-to-CAFM spin-flop transition tuned by in-plane rotation of magnetic field. These complex magnetic properties suggest that interlayer magnetic coupling plays an intricate role in this material, despite its strength being trivial compared to the strength of the intralayer ferromagnetic coupling. Interlayer coupling undergoes drastic and complex changes with temperature, magnetic field, and in-plane rotation of field, accompanied by critical changes in  $c$ -axis transport, highlighting the strong spin-charge coupling in  $\text{Ca}_3\text{Ru}_2\text{O}_7$ . Further theoretical investigation is necessarily needed to reveal underlying physics of these intriguing phenomena.

#### V. ACKNOWLEDGEMENTS

This work is supported by the DOD ARO under Grant No. W911NF0910530 (support for materials), the NSF under grant DMR-0645305 (support for equipment), and the DOE under DE-FG02-07ER46358 (personnel support).

- 
- \* Electronic address: [zmao@tulane.edu](mailto:zmao@tulane.edu)
- <sup>1</sup> K. Ishida, H. Mukuda, Y. Kitaoka, K. Asayama, Z. Q. Mao, Y. Mori, and Y. Maeno, *Nature* **396**, 658 (1998).
  - <sup>2</sup> A. P. Mackenzie and Y. Maeno, *Rev. Mod. Phys.* **75**, 657 (2003).
  - <sup>3</sup> K. D. Nelson, Z. Q. Mao, Y. Maeno, and Y. Liu, *Science* **306**, 1151 (2004).
  - <sup>4</sup> S. Nakatsuji, T. Ando, Z. Q. Mao, and Y. Maeno, *Physica B* **259**, 949 (1999).
  - <sup>5</sup> I. Zegkinoglou, J. Stempfer, C. S. Nelson, J. P. Hill, J. Chakhalian, C. Bernhard, J. C. Lang, G. Srajer, H. Fukazawa, S. Nakatsuji, et al., *Phys. Rev. Lett.* **95**, 136401 (2005).
  - <sup>6</sup> V. Anisimov, I. A. Nekrasov, D. E. Kondakov, T. M. Rice, and M. Sigrist, *Eur. Phys. J B* **25**, 191 (2002).
  - <sup>7</sup> S. A. Grigera, R. S. Perry, A. J. Schofield, M. Chiao, S. R. Julian, G. G. Lonzarich, S. I. Ikeda, Y. Maeno, A. J. Millis, and A. P. Mackenzie, *Science* **294**, 329 (2001).
  - <sup>8</sup> S. A. Grigera, P. Gegenwart, R. A. Borzi, F. Weickert, A. J. Schofield, R. S. Perry, T. Tayama, T. Sakakibara, Y. Maeno, A. G. Green, et al., *Science* **306**, 1154 (2004).
  - <sup>9</sup> R. A. Borzi, S. A. Grigera, J. Ferrell, R. S. Perry, S. J. S. Lister, S. L. Lee, D. A. Tennant, Y. Maeno, and A. P. Mackenzie, *Science* **315**, 214 (2007).
  - <sup>10</sup> Y. J. Jo, L. Balicas, N. Kikugawa, E. S. Choi, K. Storr, M. Zhou, and Z. Q. Mao, *Phys. Rev. B* **75**, 094413 (2007).
  - <sup>11</sup> D. Fobes, T. J. Liu, Z. Qu, M. Zhou, J. Hooper, M. Salamon, and Z. Q. Mao, *Phys. Rev. B* **81**, 172402 (2010).
  - <sup>12</sup> G. Cao, S. McCall, J. E. Crow, and R. P. Guertin, *Phys. Rev. Lett.* **78**, 1751 (1997).
  - <sup>13</sup> G. Cao, K. Abboud, S. McCall, J. E. Crow, and R. P. Guertin, *Phys. Rev. B* **62**, 998 (2000).
  - <sup>14</sup> Y. Yoshida, S. I. Ikeda, H. Matsuhata, N. Shirakawa, C. H. Lee, and S. Katano, *Phys. Rev. B* **72**, 054412 (2005).
  - <sup>15</sup> J. S. Lee, S. J. Moon, B. J. Yang, J. Yu, U. Schade, Y. Yoshida, S. I. Ikeda, and T. W. Noh, *Phys. Rev. Lett.* **98**, 097403 (2007).
  - <sup>16</sup> F. Baumberger, N. J. C. Ingle, N. Kikugawa, M. A. Hos-sain, W. Meevasana, R. S. Perry, K. M. Shen, D. H. Lu, A. Damascelli, A. Rost, et al., *Phys. Rev. Lett.* **96**, 107601 (2006).
  - <sup>17</sup> H. L. Liu, S. Yoon, S. L. Cooper, G. Cao, and J. E. Crow, *Phys. Rev. B* **60**, 6980(R) (1999).
  - <sup>18</sup> J. F. Karpus, R. Gupta, H. Barath, S. L. Cooper, and G. Cao, *Phys. Rev. Lett.* **93**, 167205 (2004).
  - <sup>19</sup> X. N. Lin, Z. X. Zhou, V. Durairaj, P. Schlottmann, and G. Cao, *Phys. Rev. Lett.* **95**, 017203 (2005).
  - <sup>20</sup> B. Bohnenbuck, I. Zegkinoglou, J. Stempfer, C. Schler-Langeheine, C. S. Nelson, P. Leininger, H.-H. Wu, E. Schierle, J. C. Lang, G. Srajer, et al., *Phys. Rev. B* **77**, 224412 (2008).
  - <sup>21</sup> G. Cao, L. Balicas, X. N. Lin, S. Chikara, E. Elhami, V. Duairaj, J. W. Brill, R. C. Rai, and J. E. Crow, *Phys. Rev. B* **69**, 014404 (2004).
  - <sup>22</sup> G. Cao, L. Balicas, Y. Xin, E. Dagotto, J. E. Crow, C. S. Nelson, and D. F. Agterberg, *Phys. Rev. B* **67**, 060406(R) (2003).
  - <sup>23</sup> D. J. Singh and S. Auluck, *Phys. Rev. Lett.* **96**, 097203 (2006).
  - <sup>24</sup> W. Bao, Z. Q. Mao, Z. Qu, and J. W. Lynn, *Phys. Rev. Lett.* **100**, 247203 (2006).
  - <sup>25</sup> S. McCall, G. Cao, and J. E. Crow, *Phys. Rev. B* **67**, 094427 (2003).
  - <sup>26</sup> E. Cimpoeasu, V. Sandu, C. C. Almasan, A. P. Paulikas, and B. W. Veal, *Phys. Rev. B* **65**, 144505 (2002).
  - <sup>27</sup> C. Gould, C. Ruster, T. Jungwirth, E. Girgis, G. M. Schott, R. Giraud, K. Brunner, G. Schmidt, and L. W. Molenkamp, *Phys. Rev. Lett.* **93**, 117203 (2004).
  - <sup>28</sup> G. P. Moore, J. Ferre, A. Mougin, M. Moreno, and L. Daweritz, *J. Appl. Phys.* **94**, 4530 (2003).
  - <sup>29</sup> J. Moser, A. Matos-Abiague, D. Schuh, W. Wegscheider, J. Fabian, and D. Weiss, *Phys. Rev. Lett.* **99**, 056601 (2007).
  - <sup>30</sup> X. L. Ke, J. Peng, and Z. Q. Mao, private communication (2010).
  - <sup>31</sup> J. Peng, Z. Qu, B. Qian, D. Fobes, T. Liu, X. Wu, H. M. Pham, L. Spinu, and Z. Q. Mao, *Phys. Rev. B* **82**, 024417 (2010).
  - <sup>32</sup> E. Ohmichi, Y. Yoshida, S. I. Ikeda, N. Shirakawa, and T. Osada, *Phys. Rev. B* **70**, 104414 (2004).